Heliyon 9 (2023) e21675

Contents lists available at ScienceDirect

Heliyon

journal homepage: www.cell.com/heliyon

Lead-free novel perovskite Ba_3AsI_3: First-principles insights into its electrical, optical, and mechanical properties

Pobitra Barman[a], Md. Ferdous Rahman[a,*], Md. Rasidul Islam[b,**], Mehedi Hasan[c], Mithun Chowdhury[a], M. Khalid Hossain[d], Jibon Krishna Modak[e,f], Safa Ezzine[g], Mongi Amami[g]

[a] Advanced Energy Materials and Solar Cell Research Laboratory, Department of Electrical and Electronic Engineering, Begum Rokeya University, Rangpur, 5400, Bangladesh

[b] Department of Electrical and Electronic Engineering, Bangamata Sheikh Fojilatunnesa Mujib Science & Technology University, Jamalpur, 2012, Bangladesh

[c] General Education Department, City University, Dhaka, 1216, Bangladesh

[d] Institute of Electronics, Atomic Energy Research Establishment, Bangladesh Atomic Energy Commission, Dhaka, 1349, Bangladesh

[e] Department of Physics, Bangabandhu Sheikh Mujibur Rahman Science & Technological University, Gopalgonj, 8100, Bangladesh

[f] Department of Physics, Osaka University, Osaka, Japan

[g] Department of Chemistry, College of Sciences, King Khalid University, P.O. Box 9004, Abha, Saudi Arabia

A R T I C L E I N F O

Keywords:
Density functional theory
First-principles calculation
Mechanical properties
Electronic properties
Band structure
Optical properties

A B S T R A C T

Lead-free halide perovskites are a crucial family of materials in the fabrication of solar cells. At present, Solar cells are facing several challenges such as mechanical and thermodynamic instability, toxicity, unsuitable optical parameters, bandgap, and absorption coefficient. Ba_3AsI_3 is a halide perovskite which has demonstrated good efficiency and tremendous promise for usage in solar cell applications, and it offers a possible solution to these issues. In this study, the properties of the Ba_3AsI_3 perovskite solar cell were investigated using first-principles density functional theory (FP-DFT) calculations with the CASTEP (Cambridge serial total energy package) formulation. Most of its physical qualities, including its elasticity, electrical composition, bonding, optoelectronic characteristics, and optical characteristics have not yet been explored. In this work, these unexplored properties have been thoroughly investigated using density functional theory-based computations. The Born-Huang criterion and phonon dispersion characteristics have revealed that the material is mechanically stable. The bonding nature has been investigated using the density of states curves, Mulliken population analysis, and electronic charge density. Additionally, different elastic parameters demonstrate that Ba_3AsI_3 has reasonably high machinability and is mechanically isotropic. ELATE's three-dimensional visualization and optical properties also show isotropic behavior in all directions. The band structure shows that the bandgap is direct. Based on its direct bandgap, stability, large range of absorption coefficient, and suitable optical parameters, Ba_3AsI_3 is recommended as an absorber layer for solar cell fabrication in a near future.

* Corresponding author.
** Corresponding author.
E-mail addresses: ferdous@brur.ac.bd, ferdousapee@gmail.com (Md.F. Rahman), rasidul@bsfmstu.ac.bd (Md.R. Islam).

https://doi.org/10.1016/j.heliyon.2023.e21675
Received 9 June 2023; Received in revised form 20 October 2023; Accepted 25 October 2023
Available online 2 November 2023

1. Introduction

Due to the limited resources of non-renewable energy, it is high time to find sustainable and environment-friendly renewable energy. Solar energy is one of the best solutions for that [1–4]. Nowadays, Perovskite solar cells have generated a lot of research interest in the solar energy industry for their potential advantages such as higher efficiency, lower cost, flexibility, and versatility [5–8]. Despite their many advantages, several challenges must be overcome to make this technology practical for commercial use. One major challenge is stability, as perovskite solar cells are vulnerable to degradation over time [9–13]. Toxicity is also a concern, as some perovskite solar cells contain lead and other toxic materials [14–16]. To make perovskite solar cells more environmentally friendly, the development of alternative materials that are non-toxic and more sustainable is a must [17–20]. Reproducibility is another limitation as perovskite solar cell performance can switch significantly depending on the fabrication process and materials used [21]. Scaling is still a problem since producing affordable, effective, and large-scale perovskite solar panels can be challenging. To solve all of these possible aforementioned limitations, a novel and lead-free cubic perovskite Ba_3AsI_3 has been introduced. Some unexplored opto-electronic, mechanical, and thermodynamic properties have been investigated which suggest the potential applications of this material in solar cells and other optoelectronic sectors.

Most importantly, different functionals-GGA-PBE, GGA-PBEsol, LDA-CA-PZ, *m*-GGA RSCAN, and HSE06 functionals are employed to demonstrate the consistency of these properties and strongly establish our statement about these properties. Different XC functionals have different levels of accuracy and complexity, and they make different approximations in describing the electronic interactions. According to the local density approximation (LDA), the XC potential solely depends on the electron density at a certain location in space. However, the electron density gradient is included in the generalized gradient approximation (GGA), in addition to the density itself. Therefore, the choice of XC functional can result in different values for the electronic bandgap. *Meta*-GGA functionals are an advanced type of exchange-correlation approximations in DFT. They incorporate kinetic energy density, unlike LDA and GGA, which only consider electron density. The SCAN functional is exceptional because it properly models kinetic energy density, leading to a better understanding of structural and vibrational properties in different materials [22]. Also, Hybrid functionals can reduce self-interaction errors in transition metal compounds and improve accurate predictions of electronic and electrochemical properties. HSE06 is a dependable and versatile option for enhancing the accuracy of DFT calculations, especially in investigating the electronic and structural properties of materials [23].

The band structure, electron charge density, and density of states were calculated using the self-consistent field method. The mechanical properties were evaluated using the stress-strain method. Born-Huang inequality equations [24] are used to check the compound's stability. Young's modulus (Y), shear modulus (G), bulk modulus (B), and Poisson's ratio (ν) are calculated using their associate equation. Anisotropy of its mechanical properties has been visualized using the ELATE code [25]. Ranganathan and Ostoja-Starzewski's universal anisotropy index (A^U) equation is used to determine its anisotropy. The material's response to incident photons is predicted by studying the energy-dependent optical constants. Charge density and bond population analysis were employed to demonstrate its bonding nature.

This manuscript has been divided into four sections. In section 1, an overall introduction to our research is described. In Section 2, a concise explanation of the computational techniques based on density functional theory (DFT) that were employed in this investigation is given. The results and analysis are reported and explained in Section 3. Finally, Section 4 concludes by summarizing the key findings of the present investigation and drawing conclusions.

2. Computational method

In this study, first-principles density functional theory (DFT) [26] calculations were performed using the CASTEP (Cambridge serial total energy package) formulation [27] to investigate the properties of the Ba_3AsI_3 perovskite cell. The Kohn-Sham equation [28] is utilized to get the crystalline system's ground state. The geometric optimization was done first and then the electronic properties were calculated using the norm-conserving pseudopotentials [29] with the Broyden Fletcher Goldfarb Shanno (BFGS) [30] algorithm. To better understand the characteristics of the Ba_3AsI_3 perovskite cell generalized gradient approximation (GGA) [31] and Perdew–Burke–Ernzerhof (PBE) are used.

For this study, we employed convergence criteria including the cutoff energy of 800 eV, an SCF tolerance of 1.0 × 10-6 eV/atom, a maximum force of 0.05 eV/atm, a maximum energy of 2.0×10^{-5} eV/atom, and a maximum displacement of 0.0002 Å.To ensure the precision of calculations, a 7 × 7 × 7 k-point mesh employing the Monkhorst-Pack scheme [32] has been considered for Brillouin zone sampling. The self-consistent field approach was employed to calculate the band structure and density of states, and the parameters of the electron charge density were also established. For the extensive study, GGA-PBEsol [33] and LDA-CA-PZ [34], *m*-GGA RSCAN [35], and HSE06 functionals have been used for geometric optimization, where the geometric optimization and electronic structure properties were calculated using the OTFG ultrasoft pseudopotentials [36] with the Broyden Fletcher Goldfarb Shanno (BFGS) [30] algorithm. The optimized energy cut-off is found at 800 eV. For optical properties, the linear response approach is utilized to calculate the dielectric function's dependency on the frequency. Further, the real and imaginary components of the refractive index, conductivity, and dielectric constant were also calculated. The phonon dispersion curve and phonon density of states have been determined [37,38] using the finite displacement (FDM) approach based on the density functional perturbation theory (DFPT). The stress-strain approach was used to study the mechanical and elastic characteristics with a cut-off energy of 800 eV, a k-point mesh of 7 × 7 × 7, and an SCF tolerance of 1.0×10^{-6} eV/atom. The single crystal elastic constants, C_{ij} of the cubic structure were computed using the stress-strain method [39]. Three unique elastic constants in a cubic crystal (C_{11}, C_{44}, and C_{12}) are derived from symmetry considerations. The single crystal elastic constants C_{ij} values are used to calculate the bulk modulus (B) and shear modulus (G) using the Voigt

-Reuss-Hill (VRH) method [40,41]. To better comprehend the electronic structure of Ba_3AsI_3, a population analysis was performed. The choice of the CASTEP package and the aforementioned settings were based on previous studies that have shown their effectiveness in accurately predicting the properties of similar materials. The use of norm-conserving pseudopotentials and GGA exchange-correlation functional is a widely accepted method for DFT calculations [9,42]. The chosen convergence criteria and k-point mesh size were determined through convergence tests to ensure the accuracy and efficiency of the calculations. Overall, these computational methods were selected to ensure the high accuracy and reliability of the results obtained. Overall, this computational methodology provides a comprehensive analysis of the properties of Ba_3AsI_3 material and might be a helpful resource for further research.

3. Results and analysis

3.1. Structural properties

Ba_3AsI_3's crystal structure is a structure of an A_3MX_3-type cubic perovskite cell along with space group Pm-3m (No. 221) [43–49]. The unit cell contains three Ba, one As, and three I atoms. The positions of each atom [50] after geometric optimization are presented in Table 1. The unit cell of Ba_3AsI_3 is depicted in Fig. 1. The calculated lattice parameters are found to be in excellent agreement with the experimental data [51] that is currently available and other findings from the literature. The estimated lattice parameters are tabulated in Table 2.

3.2. Electronic properties

3.2.1. Band structure

The electronic band structure is a fundamental concept in solid-state physics that may be used to explain a range of electrical, optical, and magnetic characteristics of materials. A piece of precise information can be obtained on the optimal use in the areas of optics and electronics from Ba_3AsI_3's electronic band structure [52]. Based on the stable lattice constants, the electronic band structures were calculated. The energy (E-E_F) dependent electronic band structure for Ba_3AsI_3 in the k-space along high symmetry (X-R-*M*-G-R) directions has been calculated. For details study, GGA-PBE, GGA-PBEsol, and LDA-CA-PZ functionals are also used to perform electronic band structure. The blue dot line along the horizontal indicates the Fermi level (E_F) at 0 eV.

The blue-colored lines shown below and above energy level E_F display the valence band (VB) and conduction band (CB) respectively. The maximum point of the valence band and the minimum point of the conduction band minima take place on the identical k points indicating the direct bandgap characteristics of Ba_3AsI_3. Using GGA-PBE functionals, the direct bandgap was found to be 0.834eV at symmetry point G, given in Fig. 2(a). To explore the Band structure in greater depth, additionally, GGA-PBEsol and LDA-CA-PZ functionals were also employed. Using GGA-PBEsol functional, the maximum band energy of the valence region lies at 0 eV in the k point G. The minimum energy of the conduction region is 0.604 eV, at the same symmetry point above the Fermi level. In this case, the bandgap is also direct and has the value of 0.604 eV at symmetry point G, depicted in Fig. 2(b). Using LDA-CA-PZ functionals, the estimated maximum band energy of the valence region lies at 0 eV in the k point G. The minimum energy of the conduction region is found at 0.611 eV, at the same symmetry point above the Fermi level. Here again, the calculated bandgap is direct in nature with a value of 0.611eV at symmetry point G, illustrated in Fig. 2(c). The calculated direct bandgap of Ba_3AsI_3 is 0.59 eV and 1.35 eV for *meta*-GGA-RSCAN and hybrid HSE06 respectively and shows Fig. 2(d) and (e). The effect of SOC was also checked in the case of the GGA-PBE functional. Without SOC the value of the bandgap was 0.834 eV, whereas including SOC it was changed to 0.77 eV and shows **Fig. 2(f).**

Here, the calculation shows the difference in bandgap for using different functionals. Various exchange-correlation (XC) functionals are used in density functional theory (DFT) computations that can significantly affect the calculated bandgap value. This is because the XC functional is responsible for describing the exchange and correlation interactions between electrons in a material. The high absorption coefficient of direct bandgap materials enables them to absorb light more effectively and produce more electrical current. In addition, they have higher efficiency in converting light into electricity. These substances are perfect for usage in electrical and optoelectronic devices due to their high electron mobility and effective light emission characteristics.

Table 1
Ba_3AsI_3's estimated lattice parameter.

Element	Position		
	x	y	z
Ba	0.5	0	0
	0	0.5	0
	0	0	0.5
As	0	0	0
I	0	0.5	0.5
	0.5	0	0.5
	0.5	0.5	0

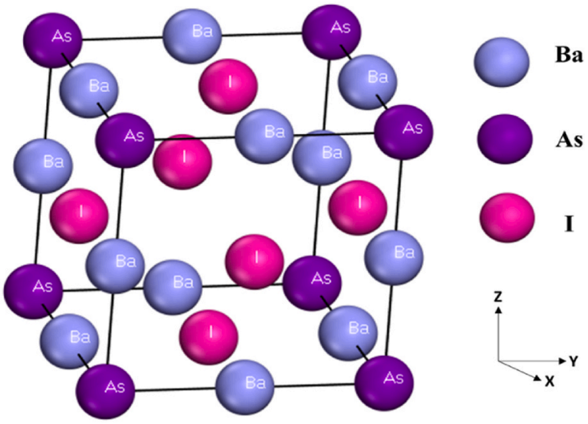

Fig. 1. Ba_3AsI_3's crystal structure and crystallographic direction.

Table 2
Calculated lattice parameter (Å), Cell volume (Å^3), and the total number of atoms of Ba_3AsI_3 crystal structure.

Compound	a	V_0	Atom number per unit cell	Functionals
Ba_3AsI_3	6.94	334.25	7	Previous work [51]
	6.89	327.93	7	GGA-PBE
	6.79	313.25	**7**	GGA-PBEsol
	6.71	301.85	**7**	LDA-CA-PZ

3.2.2. The density of states (DOS)

The Density of States (DOS) describes the distribution of energy states of electrons in a material. A visualization showing the number of electronic phases per unit of energy is known as the DOS that are available for electrons to occupy [42,53] and is shown in Fig. 3(a–c). The DOS can be used to understand the conductivity, magnetism, and optical properties of materials. All atoms' contribution to the total DOS at the Fermi level is minimal, while the valence band properties are significantly influenced by the Ba-p, As-p, and I-p orbitals. The conduction characteristics are dominated by electrons in the Ba-d, As-d, and I-d orbitals. The valence band is separated into three energy levels to better comprehend the contributions of various electronic states. The hybridization of Ba-p, As-p, I-p, Ba-s, As-s, I-s, and Ba-d, As-d, I-d produces the DOS in the lowest energy domain (−8 eV–0 eV), with Ba-p, As-p, I-p states being the predominant contribution. The conduction band energy ranges from 0 eV to 8 eV, the hybridization of Ba-s, As-s, I-s, Ba-d, As-d, and I-d contributes, with electrons from Ba-d, As-d, I-d states dominating.

3.2.3. Electronic charge density

To explain the electron's transfer and show the nature of atom-to-atom bonding in Ba_3AsI_3, the charge density distribution has been constructed. The three-dimensional and two-dimensional views of charge density are visualized in Fig. 4(a) and Fig. 4(b) respectively.

The intensity of electron density is depicted on the right rainbow-colored scale. The red color denotes the highest and the blue color denotes the lowest intensity of electron density, respectively. The sharing of charges between two atoms demonstrates covalent bonds, whereas ionic bonds are indicated by the balance of positive or negative charges at the atomic position [54]. Uniform charge distribution indicates the metallic bonding of the material. The maximum electron density is seen surrounding Ba atoms and the minimum in the I atom. The balancing positive and negative charges are seen among the Ba, As, and I atoms. This suggests that the atoms of Ba–As, and Ba–I are connected by an ionic bond. The bond population analysis agrees with this.

3.3. Mechanical properties

The elastic constant identifies a material's mechanical stability, hardness, stiffness, ductile-brittle behavior, and machinability index [14]. A list of derived elastic constants is presented in Table 3. As Ba_3AsI_3 is cubic in nature, it has three independent elastic constants (C_{ij}). To ensure mechanical stability, a system must satisfy specific inequality conditions outlined in the Born-Huang criteria using equation (1) [24].

$$C_{11} - |C_{12}| > 0 \tag{1}$$

$$(C_{11} + C_{12})C_{33} - 2C_{13}^2 > 0$$

$$C_{44} > 0$$

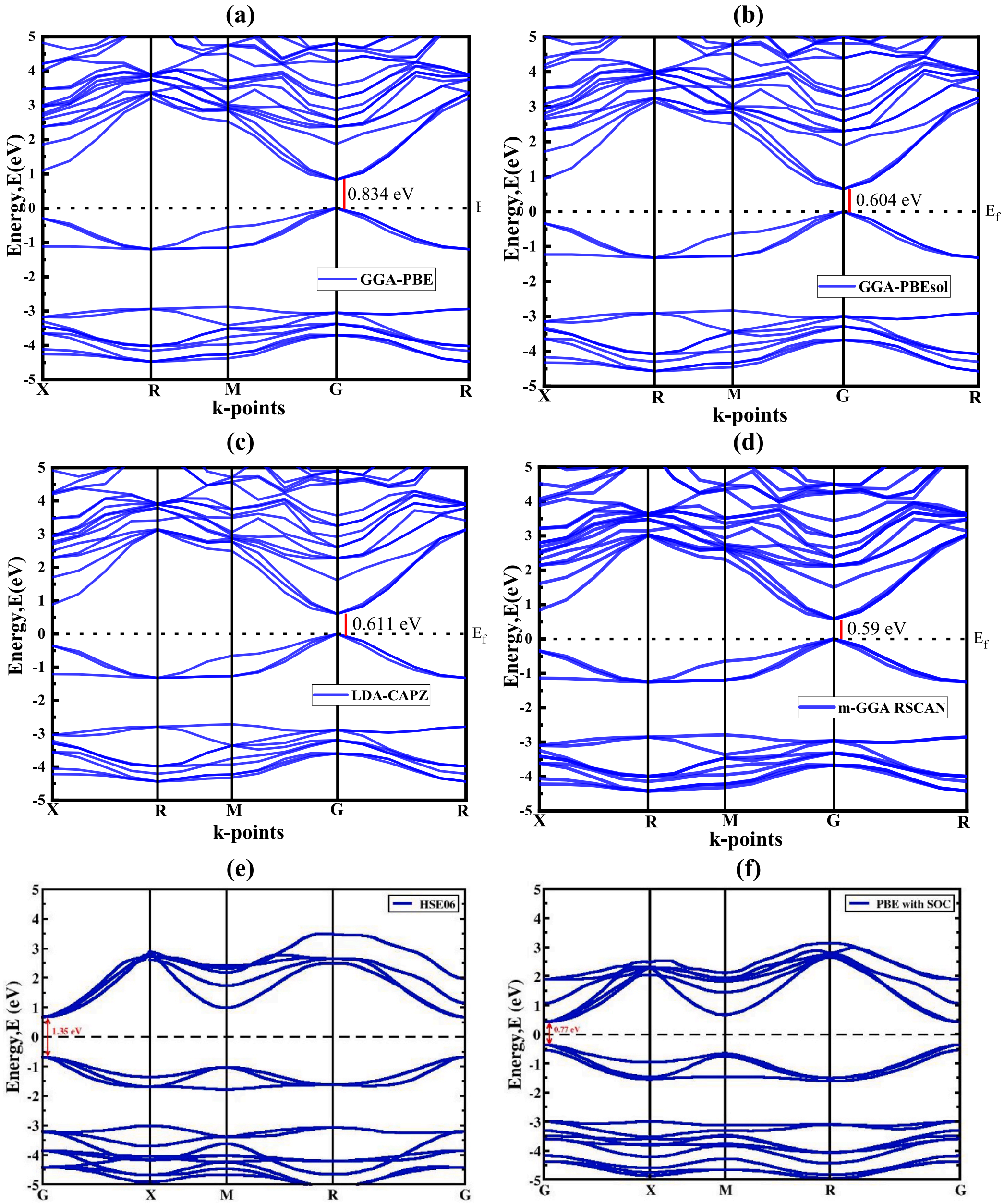

Fig. 2. Ba_3AsI_3's band structure using (a) GGA-PBE (b) GGA-PBEsol (c) LDA-CAPZ, (d) *m*-GGA RSCAN, (e)HSE06 functionals, and (f) SOC effect.

As the elastic constant meets the aforementioned stability requirements, Ba_3AsI_3 is mechanically stable [55]. C_{11} determines how resistant a material is to mechanical stress applied in its crystallographic orientations. The elastic constant C_{44} represents a compound's resistance to shear deformation. Off-diagonal shear components, also known as C_{12}, are linked to a compound's resistance to Ba_3AsI_3 due to form distortions. The parameter $C^{'}$, which is equal to the resistance to shear deformation by shear stress applied in the (110) plane in the (110) direction, measures the crystal stiffness and is calculated using equation (2):

$$C^{'} = \frac{C_{11} - C_{12}}{2} \quad (2)$$

The Cauchy pressure of a compound is a crucial mechanical characteristic for describing a material. Another method to assess a material's brittleness or ductility is to look at its Cauchy pressure value. It is defined by C'' and expressed as [14] - $C'' = C_{12} - C_{44}$ where a material's ductility is indicated by a positive value and its brittleness by a negative [56].

The internal strain parameter or Kleinman parameter (ζ), commonly known as the internal strain parameter, is a parameter that can

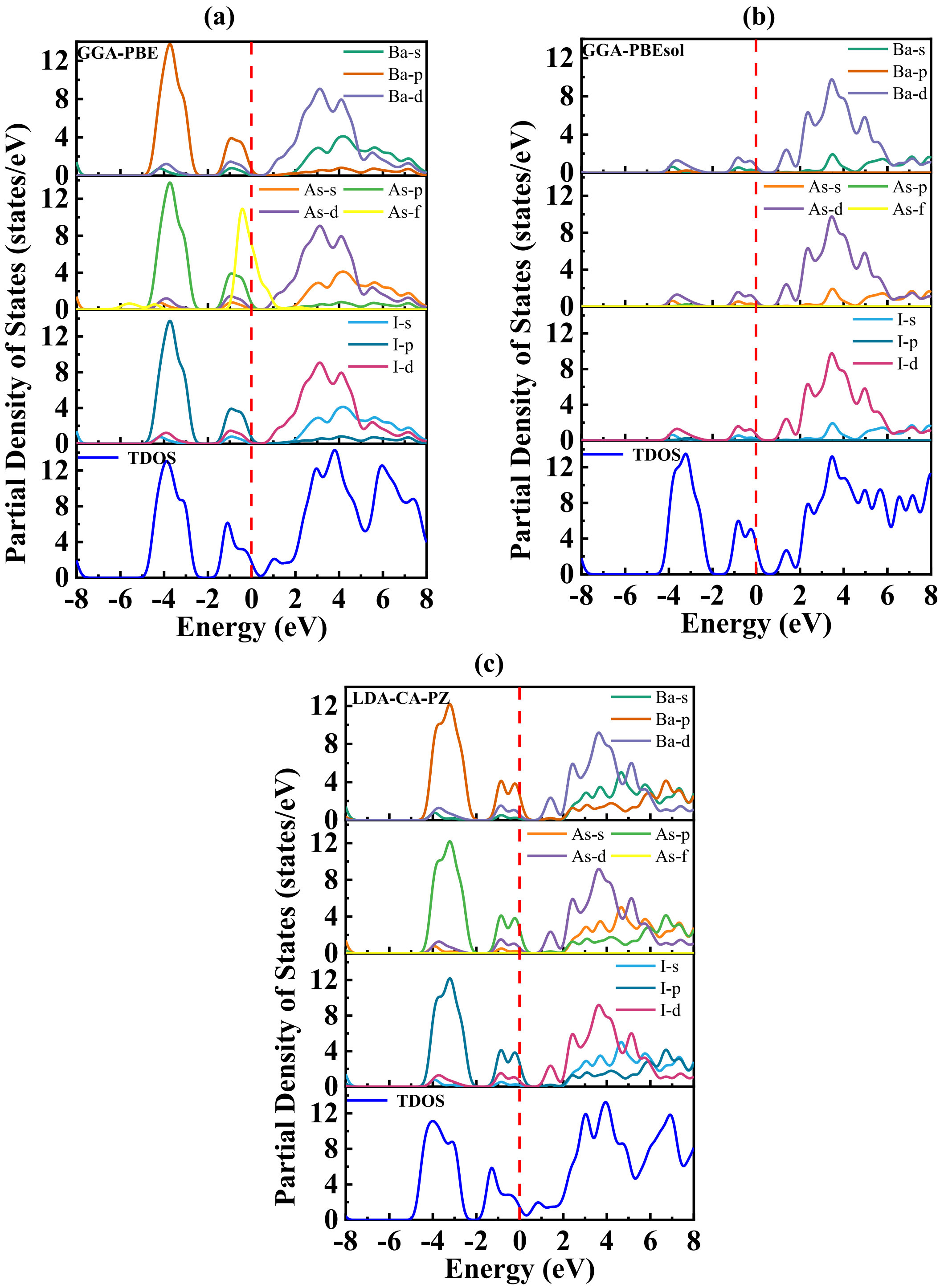

Fig. 3. Ba_3AsI_3's calculated the PDOS and TDOS using (a) GGA-PBE(b) GGA-PBEsol, and (c) LDA-CA-PZ functionals.

be used to gauge a compound's resistance to stretching and bending [57]. It is denotes by ζ and expressed as equation (3):

$$\zeta = \frac{C_{11}+8C_{12}}{7C_{11}+2C_{12}} \tag{3}$$

The lower and upper limits of the Kleinman parameter, a dimensionless quantity having values between 0 and 1, reflect the lowest contributions of bond bending and bond stretching to the resistance to external pressure, respectively.

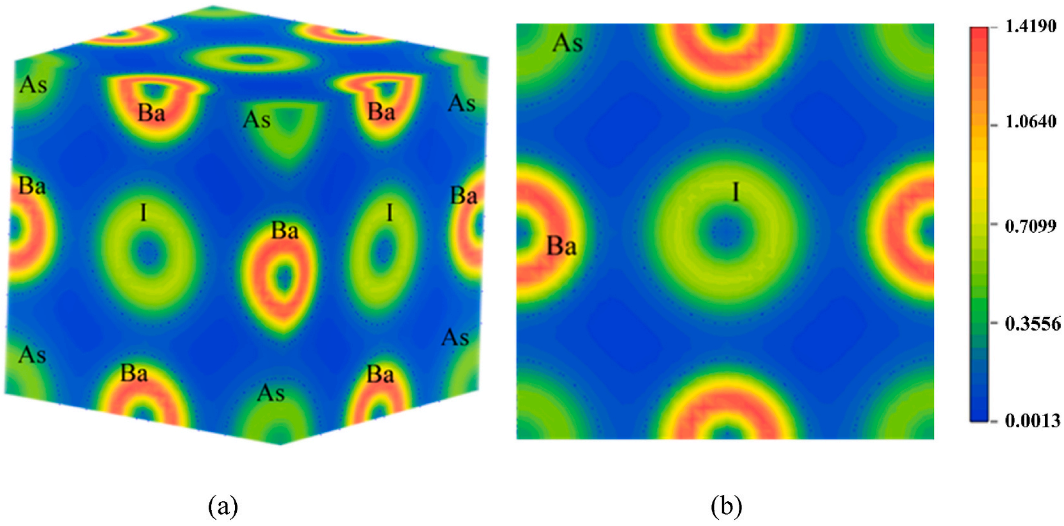

Fig. 4. The charge density (e/Å^3) of Ba_3AsI_3 (a) 3D and (b) 2D visualization.

Table 3
Ba_3AsI_3's calculated elastic constant, Cij (GPa), shear modulus C' (GPa), Cauchy pressure C' (GPa), and Kleinman parameter (ζ) using different functionals.

Compound	C_{11}	C_{12}	C_{44}	C'	C″	ζ	Functionals
Ba_3AsI_3	56.31	6.58	8.01	24.87	−1.43	0.27	GGA-PBE
	66. 09	6.71	7.54	29.69	−0.83	0.25	GGA-PBEsol
	74.32	5.85	7.55	34.24	−1.7	0.23	LDA-CA-PZ

The calculated Cauchy's pressures are −1.43 GPa, −0.83 GPa, and −1.7 GPa for the functionals GGA-PBE, GGA-PBEsol, and LDA-CA-PZ respectively. All of the values are negative and this reveals the brittleness of Ba_3AsI_3 [14]. Pettifor [58] states that with an angular shape, the Cauchy pressure is against directional bonding. Along with the value of negative Cauchy pressure, the bonding's mobility is diminishing.

The Hill approximations value [59–61] of Young's modulus (Y_H), shear modulus (G_H), bulk modulus (B), and Poisson's ratio (ν) of Ba_3AsI_3 have been assessed utilizing the usual equations of (4-7):

$$B_H = \frac{B_V + B_R}{2} \tag{4}$$

$$G_H = \frac{G_V + G_R}{2} \tag{5}$$

$$Y = \frac{9BG}{(3B + G)} \tag{6}$$

$$\nu = \frac{(3B - 2G)}{2(3B + G)} \tag{7}$$

Using the aforementioned equation, the calculated value of these terms is shown in Table 4.

Young's modulus, sometimes referred to as the modulus of elasticity, is a parameter that expresses how stiff a material is in reaction to tensile or compressive stress. Within a material's elastic range, it is described as the ratio of stress to strain. Young's modulus is

Table 4
Ba_3AsI_3 compound's calculated Young's modulus Y (GPa), shear modulus G (GPa), bulk modulus B (GPa), Pugh's indicator G/B, Machinability index μ_M, Poisson's ratio ν and hardness H (GPa) derived from the Voigt-Reuss-Hill (VRH) approximations.

	Y			G			B	B/G	μ_M	ν	H	Functionals
	Y_V	Y_R	Y_H	G_V	G_R	G_H						
Ba_3AsI_3	36.50	28.46	32.57	14.75	10.99	12.87	23.16	1.80	2.89	0.27	1.97	GGA-PBE
	40.79	28.39	34.78	16.40	10.74	13.57	26.51	1.95	3.51	0.28	1.98	GGA-PBEsol
	45.11	29.18	37.43	18.22	10.97	14.59	28.68	1.96	3.80	0.28	2.14	LDA-CA-PZ

denoted by the symbol Y and has units of pressure or stress, expressed in pascals (Pa) or gigapascals (GPa).

The resistance of a material to shear stress is gauged by its shear modulus, also known as the modulus of rigidity. It describes the proportion of shear force to shear strain within a material's elastic limit. Shear modulus is denoted by the symbol G and has units of pressure or stress, typically expressed in pascals (Pa) or gigapascals (GPa). A material's bulk modulus determines how resistant it is to compression. Within a material's elastic limit, it defines the ratio of compressive stress to volumetric strain. Bulk modulus is denoted by the symbol B and has the unit of pressure or stress, typically expressed in pascals (Pa) or gigapascals (GPa). The transverse strain to corresponding longitudinal strain ratio in a material is known as Poisson's ratio, which is a dimensionless quantity. It is an indicator of the material's deformation behavior under stress. Poisson's ratio has a critical value of 0.26 GPa [14]. Materials projected to fracture brittlely have a Poisson's ratio smaller than the critical value of 0.26, whereas those predicted to fail ductility have a Poisson's ratio higher than the critical value. For the compound Ba_3AsI_3, the computed value of v is 0.27 for GGA-PBE, 0.28 for GGA-PBEsol, and 0.28 for LDA-CA-PZ, which forecasts the compound's ductile failure and shows that the central force predominates in the atomic bonding of Ba_3AsI_3.

Pugh's ratio is a dimensionless constant that is calculated by dividing the bulk modulus of a material by its shear modulus [62–64]. It is used as another indicator of a material's brittleness or ductility. Materials with low Pugh ratios tend to be brittle, while those with high Pugh ratios tend to be ductile. The critical number for Pugh's ratio (B/G) is 1.75. Materials that have a value above the critical value show ductility, whereas those that have a value below this show brittleness. From Table 4, the estimated Pugh's ratio for Ba_3AsI_3 is 1.80 (GGA-PBE), 1.95 (GGA-PBEsol), and 1.96 (LDA-CA-PZ), which is higher than the critical value which means the compound is ductile.

Machinability is a measure of how easily a material can be machined using standard machining techniques. It is affected by factors such as the material's hardness, strength, ductility, and thermal conductivity. High machinability indicates that the material can be machined easily and efficiently, while low machinability indicates that it is more difficult and time-consuming for a machine.

The machinability index, μ_M [65] of a material is calculated using equation (8):

$$\mu_M = \frac{B}{C_{44}} \tag{8}$$

The calculated values of μ_M for Ba_3AsI_3 are 2.89 (GGA-PBE), 3.51 (GGA-PBEsol), and 3.80 (LDA-CA-PZ). Ba_3AsI_3 has a relatively high machinability index, μ_M.

3.4. Elastic anisotropy

Elastic isotropy refers to a property of a material where its elastic properties are the same in all directions. This means that when an external force is applied to that material, its mechanical properties will change in the same manner in all directions. On the other hand, a material is said to exhibit elastic anisotropy when its elastic properties vary with direction. This can occur due to structural or compositional differences in different crystallographic directions or grain orientations. Anisotropy in shear A^G and anisotropy in compressibility A^B of the compound can be determined by the following conventional equations (9) and (10):

$$A^B = \frac{B_V - B_R}{B_V + B_R} \tag{9}$$

$$A^G = \frac{G_V - G_R}{2G_H} \tag{10}$$

A universal anisotropy index (A^U) was proposed by Ranganathan and Ostoja-Starzewski. The following equation (11) determines the A^U [66,67]-

$$A^U = 5\frac{G_V}{G_R} + \frac{B_V}{B_R} - 6 \geq 0 \tag{11}$$

The values of A^B and A^G ranged from 0 to 1. $A^B = A^G = 0$ represents the perfect elastic isotropy and $A^B = A^G = 1$ represents the maximum elastic anisotropy. From Table 5 The value of A^B is 0 for all functions. So, A^B shows perfect elastic isotropy for this compound. The calculated value for anisotropy in shear A^G is 0.14, 0.20, and o.24 for the functionals GGA-PBE, GGA-PBsol, and LDA-CA-PZ respectively. It indicates a small deviation from isotropy characteristics. No matter the symmetry of the crystal, it offers a single measure of anisotropy. A^U addresses the influence of the solid's bulk on a small anisotropy, in contrast to all other anisotropy indices. The A^U provides zero or positive values, where zero represents isotropy and positive values for the anisotropy characteristics of the material. The determined values for A^U are 1.7, 2.6, and 3.3 for the functionals GGA-PBE, GGA-PBsol, and LDA-CA-PZ respectively. The

Table 5
The universal anisotropy index A^U, anisotropy in shear A^G, and anisotropy in compressibility A^B of Ba_3AsI_3.

Functional	B_V	B_R	G_V	G_R	G_H	A^B	A^G	A^U
GGA-PBE	23.16	23.16	14.75	10.99	12.87	0	0.14	1.7
GGA-PBEsol	26.51	26.51	16.40	10.74	13.57	0	0.20	2.6
LDA-CA-PZ	28.68	28.68	18.22	10.97	14.59	0	0.24	3.3

studied compound is mechanically a small anisotropic.

Using the ELATE code, Young's modulus, shear modulus, and Poisson's ratio's direction-dependent have been constructed [25] to further illustrate elastic isotropy. A three-dimensional representation of an isotropic crystal must be spherical. The shift from spherical shows the degree of anisotropy. Fig. 5(a-c), Fig. 6(a–c), and Fig. 7(a-c) display the isotropic nature of this material.

3.5. Optical properties

Optical properties refer to how a material interacts with light, including its behavior when exposed to light and its ability to manipulate light. A substance's optical properties are determined by how photons that are incident on its surface interact with that substance. The interest in the optical properties of materials has grown significantly over the past few decades as a result of the close relationships between these properties and integrated optics applications such as optical modulation, optoelectronics, optical information processing, and communications [14,53].

The response of the incident photons is seen to have the following properties: Dielectric function ε(ω), optical conductivity σ(ω), refractive index N(ω), absorption coefficient α(ω), reflectivity R(ω), and loss function L(ω). For photon energies up to 30 eV, the optical properties of Ba_3AsI_3 for incident polarization directions [100] and [001] have been calculated and illustrated. The optical properties of Ba_3AsI_3 that are dependent on photon energy have been determined using intricate dielectric functions. The complex dielectric function is calculated using equation (12) [68]:

$$\varepsilon(\omega) = \varepsilon_1(\omega) + i\varepsilon_2(\omega) \tag{12}$$

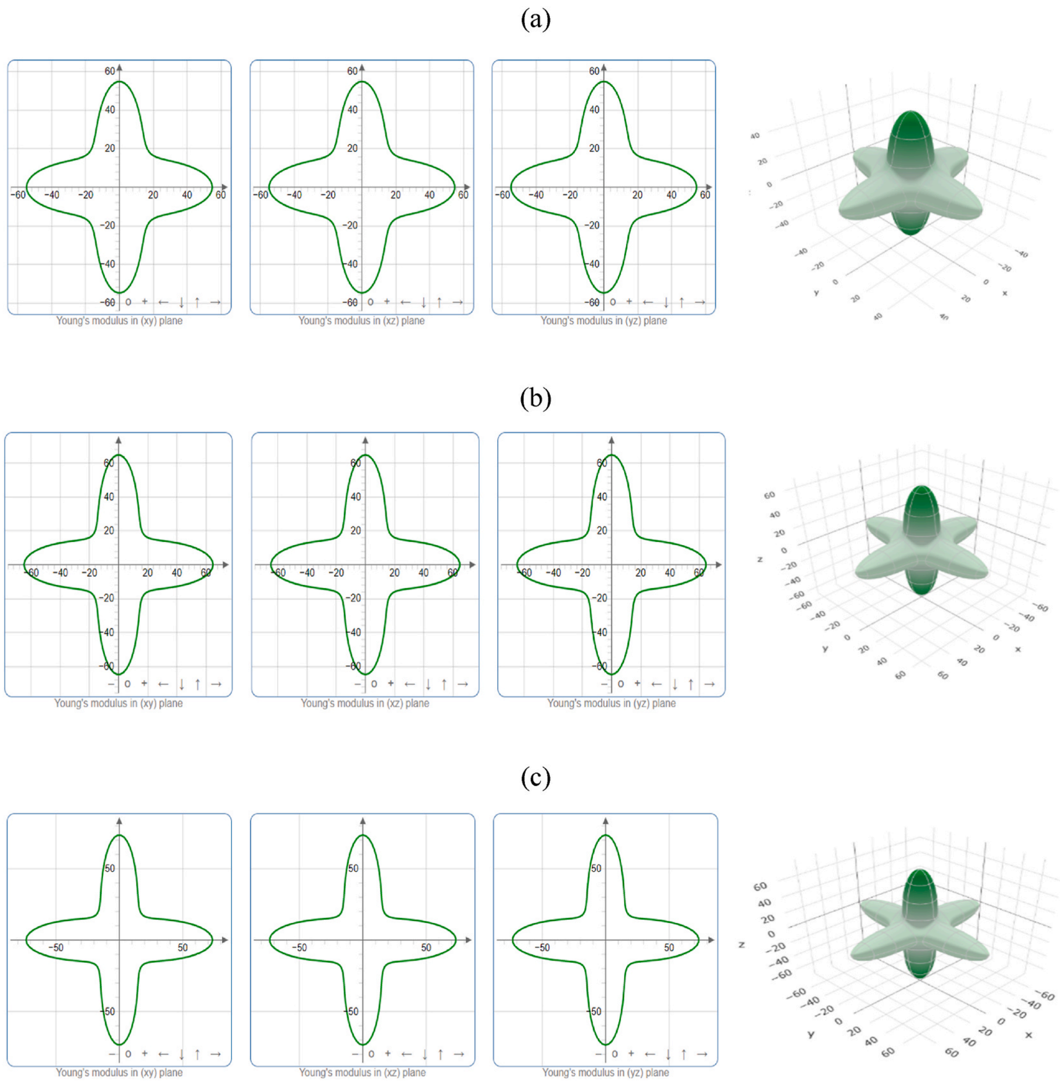

Fig. 5. 2D and 3D visualization of Young's modulus using (a) GGA-PBE, (b) GGA-PBEsol, and(c) LDA-CA-PZ functionals.

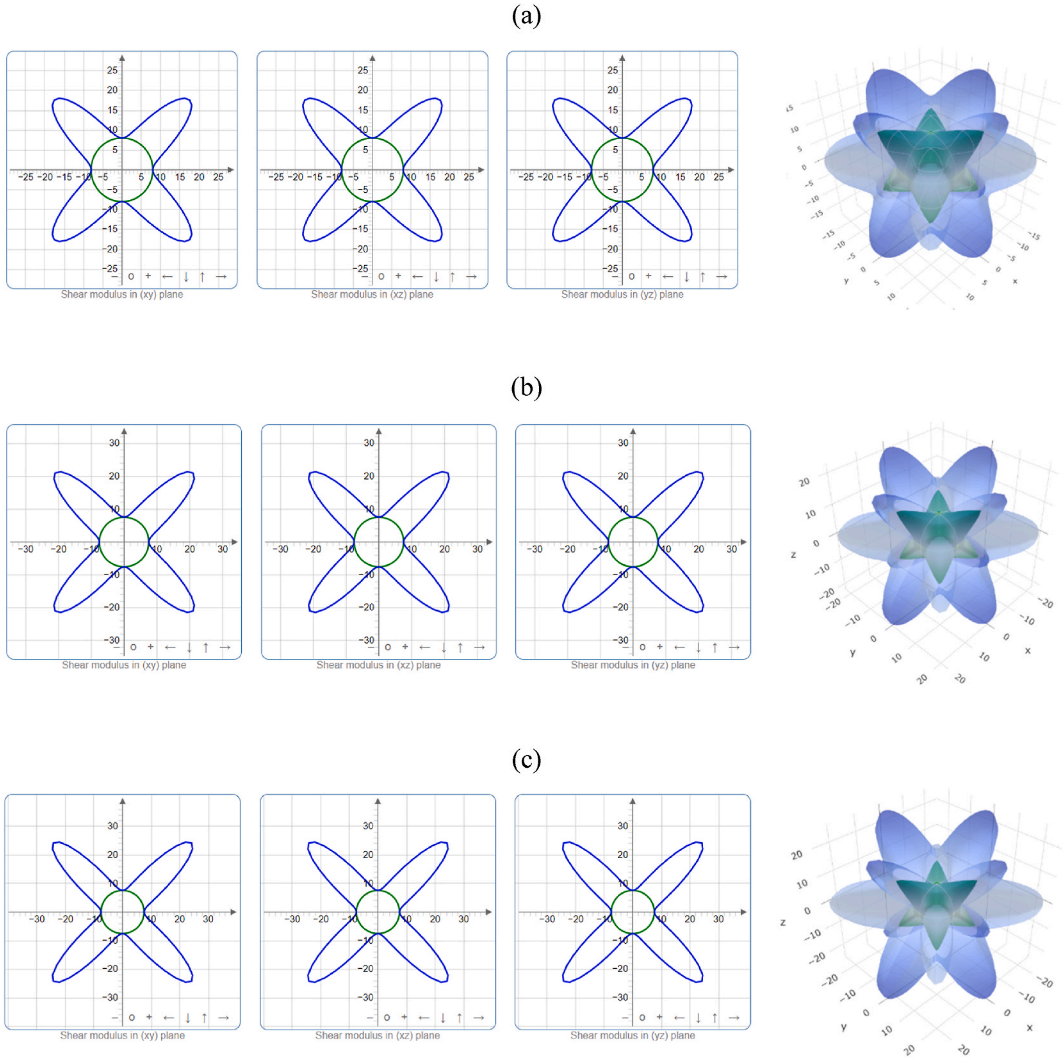

Fig. 6. 2D and 3D visualization of Shear modulus using (a) GGA-PBE, (b) GGA-PBEsol, and (c) LDA-CA-PZ functionals.

The polarizability of the material is shown by the real portion of the dielectric function, while the imaginary portion shows its absorptive activity. Polarization and dispersion effects are reflected in the dielectric constant's real portion. The material's frequency-dependent dielectric functions are illustrated in Fig. 8(a). The real part's $\varepsilon_1(\omega)$ finest basic factor is $\varepsilon_1(0)$. The real part crosses zero at ~7eV (GGA-PBE), 7.5eV (GGA-PBEsol), and 7.5eV (LDA-CA-PZ). It becomes unity after 7eV. Yet, beyond 7 eV, the imaginary portion practically reaches zero. Positive values of the $\varepsilon_1(\omega)$ function for Ba_3AsI_3 show that it is highly reflective and semiconducting.

Optical conductivity $\sigma(\omega)$ is depicted in Fig. 8(b). The material exhibits its photoconductivity after 0.834 eV (GGA-PBE), 0.645 eV (GGA-PBEsol), and 0.611 eV (LDA-CA-PZ) in Fig. 8(b). So, the material shows photoconductivity after crossing its bandgap energy. This phenomenon demonstrates that Ba_3AsI_3 is a semiconductor. The graph abruptly increases after the bandgap energy from 0.834 eV to 7eV and 13eV to 17 eV. Two peak values of photoconductivity 5.17 and 4.07 for 6.9 eV and 16.8 eV are found for GGA-PBE, GGA-PBEsol, and 5.15 for 6.92 eV LDA-CA-PZ functional respectively. Photoconductivity decreases in the energy range 7–13eV and 17–31eV. It becomes zero at 30 eV. From 0.834 to 32 eV, Ba_3AsI_3 exhibits a broad photoconductivity photon energy range. It indicates that Ba_3AsI_3 is a good photoconductive material.

The amount of light bending or deflecting as it travels through a substance is measured by the refractive index. This value is unique to each material and can be used to predict how light will behave as it passes through it, such as how much it will bend, reflect, or be absorbed. The complex refractive index is defined as $N(\omega)$.

The refractive index is given by equation (13):

$$N(\omega) = n(\omega) + ik(\omega) \tag{13}$$

where the imaginary portion of $N(\omega)$ is known as the extinction coefficient. The extinction coefficient, k (imaginary portion) spectrum

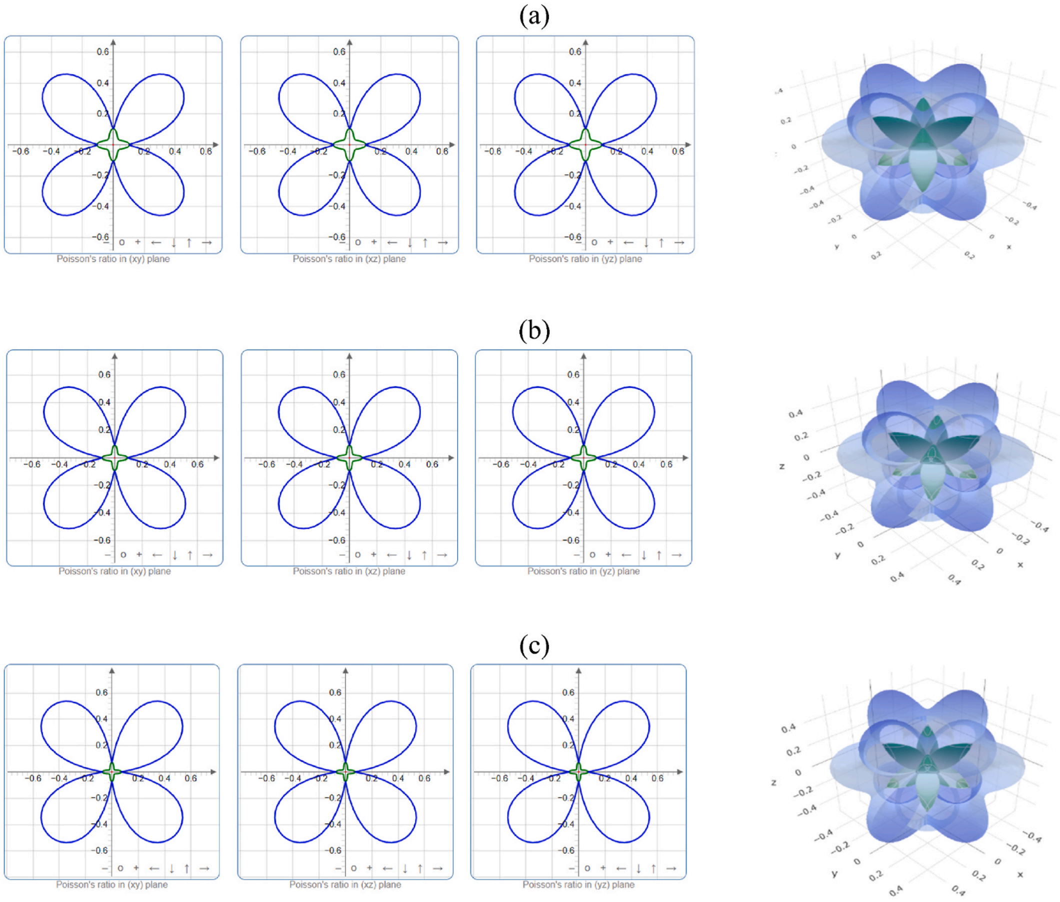

Fig. 7. 2D and 3D visualization of Poisson's ratio using (a) GGA-PBE, (b) GGA-PBEsol, and (c) LDA-CA-PZ functionals.

describes the amount of attenuated incident electromagnetic radiation when it passes through the material, whereas the real part, n shows the electromagnetic wave's phase velocity. One of the most important parameters for photoelectronic devices is the extinction coefficient n(k). The incident photon energy-dependent refractive index is shown in Fig. 8(c) for GGA-PBE, GGA-PBEsol, and LDA-CA-PZ functionals respectively. According to the calculations shown in Fig. 8(c) the static refractive index, n (0) has values of 2.78, 2.75, and 2.76, respectively. The refractive index is suitable for optoelectronic devices, such as lasers, photodetectors, LED, and photovoltaics.

The absorption coefficient reveals a substance's capacity to absorb incident radiation. The Absorption coefficient's dependency on photon energy (eV) is shown in Fig. 8(d). The different functionals used to perform absorption coefficient calculation. Due to its semiconducting nature and expected band gap, the curve of Ba_3AsI_3 that is involved with the best solar energy conversion efficiency starts at about 0.84 eV and is depicted by the band diagram beginning at that same stage of energy. Across the spectral band from about 5 eV to 11 eV, 15 eV–20 eV, the absorption coefficient is fairly high, peaking at about a photon energy of 17.6 eV. It becomes zero after 29 eV. From the photon energy range 0.834–29 eV, Ba_3AsI_3 exhibits a broad absorption coefficient. It suggests that Ba_3AsI_3 is an excellent material for absorption.

Fig. 8(e) demonstrates that the static component of reflectivity is the R(ω) and begins at zero energy. Additionally, for this solar cell absorber, R(0) is noted to be 0.24. The intra-band transition in the compound has a maximum reflectivity is 0.3 in the infrared range, 3.85 eV. The observed reflectivity decreases as the material's energy band gap increases. It becomes zero after 30 eV. So, Ba_3AsI_3 shows reflectivity in a small amount. It indicates that Ba_3AsI_3 uses in optoelectronic devices.

The loss function's L(ω) dependency on photon energy (eV) is illustrated in Fig. 8(f). The loss function graph displays how the material reacts to an electromagnetic wave concerning its energy. The loss function, often known as the dielectric function's imaginary component, simulates how a semiconductor absorbs light. This phenomenon demonstrates that Ba_3AsI_3 is a semiconductor. The loss function is almost zero at low photon energies because there isn't enough energy in the photon to cause any electronic transitions to occur in the material. The loss function starts to rise as the photon energy increases, showing that the semiconductor is beginning to absorb the incident light. For GGA-PBe functional, the graph abruptly increases after 17 eV. Two peak values of loss function are 3.55 and 1.02 eV for 21.7 eV and 12.5 eV respectively. It becomes zero after 28 eV. The abrupt loss peak is an illustration of the rapid decrease in Ba_3AsI_3's reflectivity and absorption coefficient.

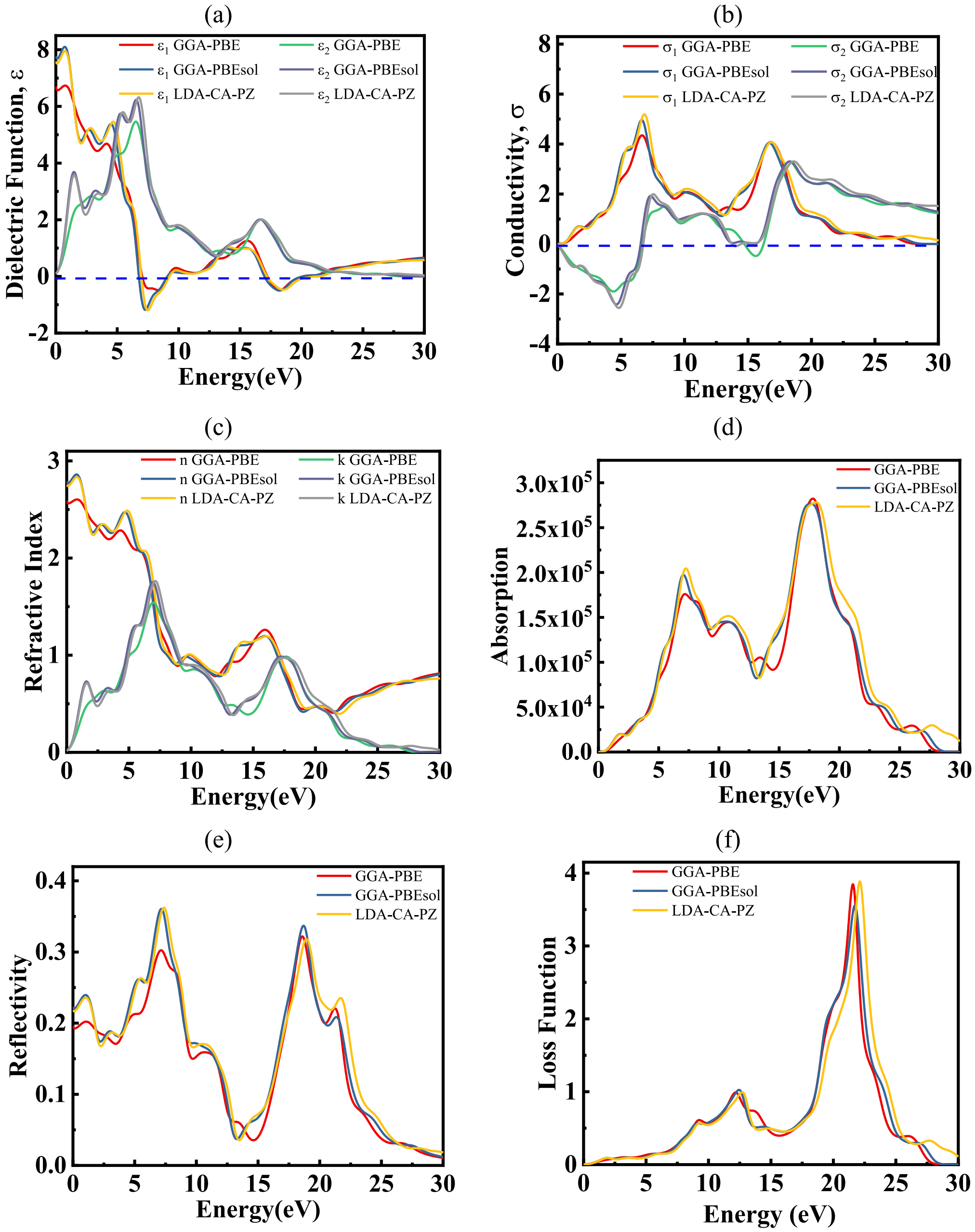

Fig. 8. (a) Dielectric function, (b) Conductivity, (c) Refractive index, (d) Absorption, (e) Reflectivity, and (f) Loss function's dependency on photon energy (eV) using different functionals.

3.6. Bond population analysis

The electron density distribution of a molecule can be described using the popular technique known as Mulliken population analysis (MPA) [69]. MPA defines the nature of bonding (ionic, covalent, and metallic) in Ba_3AsI_3. The calculated population analysis charge parameters are shown in Table 6. The compound's Mulliken charges for Ba, As, and I are 0.72, −0.88, and −0.43 respectively. Here, As and I atoms receive electronic charges from Ba atoms. This demonstrates the presence of ionic bonds between some of the compound's atoms. The As and I atoms receive these charges from the d orbital of the Ba atom. The Formal ionic charge for Ba, As, and I is +2, −3, and −1 respectively. This indicates the covalent bond's presence among atoms. Ba_3AsI_3's effective valence charge (EVC) is used to calculate the degree of covalency. The difference between the formal ionic charge and the computed Mulliken charge is EVC [69,70]. A greater EVC number indicates an increasing amount of covalency [71]. Nevertheless, Due to the heavy dependence on the

Table 6
Ba_3AsI_3's calculated population analysis charge parameter; Spilling of charge (%), Atomic populations of Mulliken (electron), Charge of Mulliken (electron), formal ionic charge, effective valence charge(electron), and Hirshfeld charge (electron).

Compound	Spilling of charge	Species	Atomic populations of Mulliken				Charge of Mulliken	Formal ionic charge	effective valence charge	Hirshfeld charge
			s	p	d	Total				
Ba_3AsI_3	1.17	Ba	2.36	5.99	0.92	9.28	+0.72	+2	1.38	+0.21
		As	1.72	4.16	0	5.88	−0.88	−3	2.12	−0.48
		I	1.93	5.50	0	7.43	−0.43	−1	0.57	−0.05

basis set, MPA occasionally yields results that are inconsistent with chemical perception and considerably overestimate covalency. For these reasons, Hirshfeld population analysis (HPA) [72] was also utilized, since it rarely depends on the basis set and frequently produces more insightful findings.

3.7. Phonon dispersion curve and phonon density of states

A phonon is an aggregate excitation of atoms or molecules in a crystalline lattice that propagate the lattice as a wave in solid-state physics [73]. The relationship between the phonon energy and its wave vector is known as the phonons' dispersion relationship in a semiconductor [14].

A measurement of the number of energy levels that are accessible for use at each energy level is the density of states (DOS). The density functional perturbation theory (DFPT)-based finite displacement (FDM) approach was used to compute the phonon characteristics [37,38] shown in Fig. 9. A material's phonon dispersion spectrum (PDS) offers crucial information on dynamical stability, phase transitions, and the contributions of vibrations to characteristics like thermal expansion and heat capacity [74]. Fig. 9(a) and (b) illustrate the phonon dispersion curve and phonon density of states, respectively. The properties can be used to determine a variety of physical properties of materials. These properties also can be used to directly or indirectly identify a variety of physical characteristics of materials [75]. Phonon dispersion spectra (PDS) may be used to understand a material's structural stability, phase transition, and vibrational contribution to its thermal and charge transport properties [74]. The dynamical stability of a material is a critical factor to take into account for applications involving time-varying mechanical stress. Ba_3AsI_3's maximum vibrational frequency is found at 3.22 THz in the G point of the BZ. Around 2.37 THz, the PHDOS peaks are visible.

4. Conclusions

In this work, various physical properties such as mechanical, phonon, electronic, optical, and population analysis of lead-free cubic halide perovskite of Ba_3AsI_3 has been explored using DFT. Three different functionals (GGA-PBE, GGA-PBEsol, LDA-CA-PZ) are used for all investigation and comparison in details. Additionally, HSE06 and *m*-GGA RSCAN functionals are used for band structure calculation only due to high computational cost and more time-consuming approach. After analyzing the Born stability condition and phonon dispersion curve, it has been concluded that the compound is mechanically stable. Another favorable aspect is that it has a relatively high machinability index. However, based on the Cauchy pressure, Pugh's ratio, and Poisson's ratio, it is suggested that this material is brittle. All 3D figures generated from ELATE software also state the isotropic nature of this material. Optical properties also show isotropic behavior in all direction and the electronic band structure exhibits its semiconducting nature. According to Population

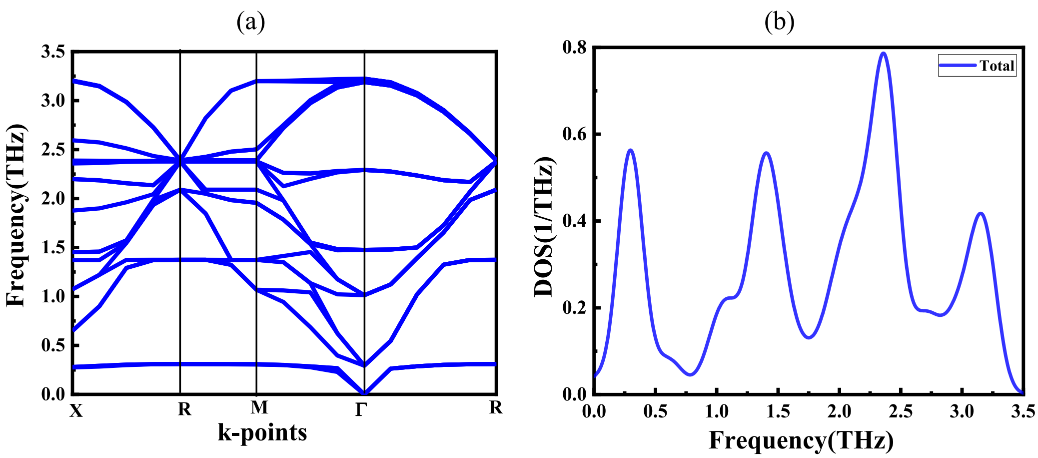

Fig. 9. Ba_3AsI_3's (a) phonon dispersion curve and (b) phonon density of states.

analysis and the electron charge density, the compound possesses ionic bonding and over a wide range of photon energies, Ba_3AsI_3 exhibits high reflectivity and absorption coefficients. Above all of these characteristic have promised well for its application in the optoelectronic devices in the industry in a near future.

Data availability

Data will be made available on request.

CRediT authorship contribution statement

Pobitra Barman: Writing – review & editing, Writing – original draft, Visualization, Validation, Methodology, Formal analysis, Data curation. **Md Ferdous Rahman:** Writing – review & editing, Writing – original draft, Visualization, Validation, Supervision, Software, Resources, Project administration, Methodology, Investigation, Formal analysis, Data curation, Conceptualization. **Md Rasidul Islam:** Writing – review & editing, Writing – original draft, Visualization, Supervision, Formal analysis, Data curation, Conceptualization. **Mehedi Hasan:** Writing – review & editing, Visualization, Validation, Formal analysis. **Mithun Chowdhury:** Writing – review & editing, Visualization, Validation, Software, Resources, Methodology. **M. Khalid Hossain:** Writing – review & editing, Visualization, Validation, Formal analysis. **Jibon Krishna Modak:** Writing – review & editing, Visualization, Validation, Software, Methodology, Investigation. **Safa Ezzine:** Writing – review & editing, Supervision, Project administration, Methodology, Funding acquisition. **Mongi Amami:** Writing – review & editing, Visualization, Validation, Supervision, Project administration, Funding acquisition.

Declaration of competing interest

The authors declare that they have no known competing financial interests or personal relationships that could have appeared to influence the work reported in this paper.

Acknowledgements

The authors have extended their appreciation to the Deanship of Scientific Research at King Khalid University, Saudi Arabia for grant this work through the Research Groups Program under grant number R.G.P.2: 233/44.

References

[1] Role of facile synthesized V2O5 as hole transport layer for CdS/CdTe heterojunction solar cell: Validation of simulation using experimental data, Superlattice. Microst. (2019), https://doi.org/10.1016/j.spmi.2019.106168.
[2] M.F. Rahman, J. Hossain, A. Kuddus, S. Tabassum, M.H.K. Rubel, M.M. Rahman, Y. Moriya, H. Shirai, A.B.M. Ismail, A novel CdTe ink-assisted direct synthesis of CdTe thin films for the solution-processed CdTe solar cells, J. Mater. Sci. 55 (2020) 7715–7730, https://doi.org/10.1007/s10853-020-04578-7.
[3] M.F. Rahman, M.M. Alam Moon, M.K. Hossain, M.H. Ali, M.D. Haque, A. Kuddus, J. Hossain, A.B. Abu, Concurrent investigation of antimony chalcogenide (Sb2Se3 and Sb2S3)-based solar cells with a potential WS2 electron transport layer, Heliyon 8 (2022), e12034, https://doi.org/10.1016/j.heliyon.2022.e12034.
[4] A. Isha, A. Kowsar, A. Kuddus, M.K. Hossain, M.H. Ali, M.D. Haque, M.F. Rahman, High efficiency Cu2MnSnS4 thin film solar cells with SnS BSF and CdS ETL layers: a numerical simulation, Heliyon 9 (2023), e15716, https://doi.org/10.1016/j.heliyon.2023.e15716.
[5] E. Lamanna, M. Tucci, E. Lamanna, F. Matteocci, E. Calabro, L. Serenelli, E. Salza, L. Martini, F. Menchini, M. Izzi, A. Agresti, S. Pescetelli, S. Bellani, Mechanically Stacked , Two-Terminal Graphene-Based Perovskite/Silicon Tandem Solar Cell with Efficiency over 26 % Mechanically Stacked , Two-Terminal Graphene-Based Perovskite/Silicon Tandem Solar Cell with Efficiency over 26 %, 2020, pp. 1–17, https://doi.org/10.1016/j.joule.2020.01.015.
[6] D.I. Kim, J.W. Lee, R.H. Jeong, J.H. Boo, A high-efficiency and stable perovskite solar cell fabricated in ambient air using a polyaniline passivation layer, Sci. Rep. 12 (2022) 1–10, https://doi.org/10.1038/s41598-021-04547-3.
[7] A.F. Palmstrom, G.E. Eperon, T. Leijtens, R. Prasanna, S.N. Habisreutinger, W. Nemeth, E.A. Gaulding, S.P. Dunfield, M. Reese, S. Nanayakkara, T. Moot, J. Werner, J. Liu, B. To, S.T. Christensen, M.D. McGehee, M.F.A.M. van Hest, J.M. Luther, J.J. Berry, D.T. Moore, Enabling flexible all-perovskite oandem solar cells, Joule 3 (2019) 2193–2204, https://doi.org/10.1016/j.joule.2019.05.009.
[8] H.S. Jung, N.G. Park, Perovskite solar cells: from materials to devices, Small 11 (2015) 10–25, https://doi.org/10.1002/smll.201402767.
[9] M.K. Hossain, A.A. Arnab, R.C. Das, K.M. Hossain, M.H.K. Rubel, M.F. Rahman, H. Bencherif, M.E. Emetere, M.K.A. Mohammed, R. Pandey, Combined DFT, SCAPS-1D, and wxAMPS frameworks for design optimization of efficient Cs2BiAgI6-based perovskite solar cells with different charge transport layers, RSC Adv. 12 (2022) 34850–34873, https://doi.org/10.1039/d2ra06734j.
[10] M.K. Hossain, G.F.I. Toki, J. Madan, R. Pandey, H. Bencherif, M.K.A. Mohammed, M.R. Islam, M.H.K. Rubel, M.F. Rahman, S. Bhattarai, D.P. Samajdar, A comprehensive study of the optimization and comparison of cesium halide perovskite solar cells using ZnO and Cu2FeSnS4 as charge transport layers, New J. Chem. 47 (2023) 8602–8624, https://doi.org/10.1039/d3nj00320e.
[11] M.K. Hossain, G.F.I. Toki, I. Alam, R. Pandey, D.P. Samajdar, M.F. Rahman, M.R. Islam, M.H.K. Rubel, H. Bencherif, J. Madan, M.K.A. Mohammed, Numerical simulation and optimization of CsPbI3-based perovskite solar cell to enhance the power conversion efficiency, New J. Chem. 47 (2023) 4801–4817, https://doi.org/10.1039/d2nj06206b.
[12] M.K. Hossain, S. Bhattarai, A.A. Arnab, M.K.A. Mohammed, R. Pandey, H. Ali, F. Rahman, R. Islam, D.P. Samajdar, J. Madan, H. Bencherif, D.K. Dwivedi, M. Amami, RSC Advances Harnessing the potential of CsPbBr 3 -based perovskite solar cells using e ffi cient charge transport materials and global optimization, RSC Adv. 13 (2023) 21044–21062, https://doi.org/10.1039/D3RA02485G.
[13] M.K. Hossain, M.S. Uddin, G.F.I. Toki, M.K.A. Mohammed, R. Pandey, J. Madan, F. Rahman, R. Islam, S. Bhattarai, H. Bencherif, D.P. Samajdar, M. Amami, D. K. Dwivedi, RSC Advances Achieving above 24 % e ffi ciency with non-toxic potential of the absorber and charge transport, RSC Adv. 13 (2023) 23514–23537, https://doi.org/10.1039/D3RA02910G.
[14] M. Hasan, S. Nasrin, M.N. Islam, A.K.M.A. Hossain, First-principles insights into the electronic, optical, mechanical, and thermodynamic properties of lead-free cubic ABO3[A = Ba, Ca, Sr; B = Ce, Ti, Zr] perovskites, AIP Adv. 12 (2022), https://doi.org/10.1063/5.0104191.

[15] M.K. Hossain, M.H.K. Rubel, G.F.I. Toki, I. Alam, M.F. Rahman, H. Bencherif, Effect of various electron and hole transport layers on the performance of CsPbI 3 -based perovskite solar cells: a numerical investigation in DFT, SCAPS-1D, and wxAMPS frameworks, ACS Omega 7 (2022) 43210–43230, https://doi.org/10.1021/acsomega.2c05912.
[16] H. Luo, P. Li, J. Ma, X. Li, H. Zhu, Y. Cheng, Q. Li, Q. Xu, Y. Zhang, Y. Song, Bioinspired 'cage traps' for closed-loop lead management of perovskite solar cells under real-world contamination assessment, Nat. Commun. 14 (2023) 4730, https://doi.org/10.1038/s41467-023-40421-8.
[17] Z. Shi, J. Guo, Y. Chen, Q. Li, Y. Pan, H. Zhang, Y. Xia, W. Huang, Lead-free rrganic–inorganic hybrid perovskites for photovoltaic applications: aecent pdvances and oerspectives, Adv. Mater. 29 (2017), https://doi.org/10.1002/adma.201605005.
[18] M.K. Hossain, G.F.I. Toki, A. Kuddus, M.H.K. Rubel, M.M. Hossain, H. Bencherif, F. Rahman, R. Islam, M. Mushtaq, An extensive study on multiple ETL and HTL layers to design and simulation of high - performance lead - free CsSnCl 3 - based perovskite solar cells, Sci. Rep. (2023) 1–25, https://doi.org/10.1038/s41598-023-28506-2.
[19] X. Meng, Y. Wang, J. Lin, X. Liu, X. He, J. Barbaud, T. Wu, T. Noda, X. Yang, L. Han, Surface-controlled griented drowth of FASnI3 crystals for efficient lead-free perovskite solar cells, Joule 4 (2020) 902–912, https://doi.org/10.1016/j.joule.2020.03.007.
[20] G. Schileo, G. Grancini, Lead or no lead? Availability, toxicity, sustainability and environmental impact of lead-free perovskite solar cells, J. Mater. Chem. C 9 (2021) 67–76, https://doi.org/10.1039/d0tc04552g.
[21] B. Conings, L. Baeten, C. De Dobbelaere, J. D'Haen, J. Manca, H.G. Boyen, Perovskite-based hybrid solar cells exceeding 10% efficiency with high reproducibility using a thin film sandwich approach, Adv. Mater. 26 (2014) 2041–2046, https://doi.org/10.1002/adma.201304803.
[22] J. Kaczkowski, I. Płowaś-Korus, The vibrational and thermodynamic properties of CsPbI3Polymorphs: an improved iescription based on the SCAN meta-GGA functional, J. Phys. Chem. Lett. 12 (2021) 6613–6621, https://doi.org/10.1021/acs.jpclett.1c01798.
[23] I. Timrov, F. Aquilante, M. Cococcioni, N. Marzari, Accurate electronic properties and vntercalation ooltages of clivine-type Li-ion hathode materials from extended Hubbard functionals, PRX Energy 1 (2022) 1, https://doi.org/10.1103/prxenergy.1.033003.
[24] F. Mouhat, F.X. Coudert, Necessary and sufficient elastic stability conditions in various crystal systems, Phys. Rev. B Condens. Matter 90 (2014) 4–7, https://doi.org/10.1103/PhysRevB.90.224104.
[25] R. Gaillac, P. Pullumbi, F.X. Coudert, ELATE: an open-source online application for analysis and visualization of elastic tensors, J. Phys. Condens. Matter 28 (2016), https://doi.org/10.1088/0953-8984/28/27/275201.
[26] D.A. Dixon, Density Functional Theory, Encyclopedia of Earth Sciences Series, vols. 1–7, 2016, https://doi.org/10.1007/978-3-319-39193-9_17-1.
[27] M.D. Segall, P.J.D. Lindan, M.J. Probert, C.J. Pickard, P.J. Hasnip, S.J. Clark, M.C. Payne, First-principles simulation: sdeas, illustrations and the CASTEP code, J. Phys. Condens. Matter 14 (2002) 2717–2744, https://doi.org/10.1088/0953-8984/14/11/301.
[28] W.K. And, L.J. Sham, Self-consistent equations including exchange and correlation effects, KOREAN J. PHYSIOL. PHARMACOL. 10 (2006) 289–295.
[29] D.R. Hamann, M. Schlüter, C. Chiang, Norm-conserving pseudopotentials, Phys. Rev. Lett. 43 (1979) 1494–1497, https://doi.org/10.1103/PhysRevLett.43.1494.
[30] T.H. Fischer, J. Almlöf, General methods for geometry and wave function optimization, J. Phys. Chem. 96 (1992) 9768–9774, https://doi.org/10.1021/j100203a036.
[31] J.P. Perdew, K. Burke, M. Ernzerhof, Generalized gradient approximation made Simple, Phys. Rev. Lett. 77 (1996) 3865–3868, https://doi.org/10.1103/PhysRevLett.77.3865.
[32] H.J.M, J.D. Pack, Special points for Brillonin-zone integrations, PHYSICAL RE VIE B 7 (1976) 2156–2164, https://doi.org/10.1039/c8ta11250a.
[33] J.P. Perdew, A. Ruzsinszky, G.I. Csonka, O.A. Vydrov, G.E. Scuseria, L.A. Constantin, X. Zhou, K. Burke, Restoring the density-gradient expansion for exchange in solids and surfaces, Phys. Rev. Lett. 100 (2008), 136406, https://doi.org/10.1103/PhysRevLett.100.136406.
[34] D.M. Ceperley, B.J. Alder, Ground state of the electron gas by a stochastic method, Phys. Rev. Lett. 45 (1980) 566–569, https://doi.org/10.1103/PhysRevLett.45.566.
[35] A.P. Bartók, J.R. Yates, EPL 151 (2019), 207101, https://doi.org/10.1063/1.5128484. Journal of Chemical Physics. 151 (2019) 10–13.
[36] G.P. Francis, M.C. Payne, Finite basis set corrections to total energy pseudopotential calculations, J. Phys. Condens. Matter 2 (1990) 4395–4404, https://doi.org/10.1088/0953-8984/2/19/007.
[37] K. Parlinski, Z.Q. Li, Y. Kawazoe, First-principles determination of the soft mode in cubic ZrO2, Phys. Rev. Lett. 78 (1997) 4063–4066, https://doi.org/10.1103/PhysRevLett.78.4063.
[38] G. Kresse, J. Furthmüller, J. Hafner, Ab initio force constant approach to phonon dispersion relations of diamond and graphite, Epl 32 (1995) 729–734, https://doi.org/10.1209/0295-5075/32/9/005.
[39] D.M. Cui, R. Jia, Q. Xie, K.J. Zhao, First-principles calculations of stressed Ru2Si3, Faguang Xuebao/Chinese Journal of Luminescence 32 (2011) 907–912, https://doi.org/10.3788/fgxb20113209.0907.
[40] J.P. Watt, Hashin-Shtrikman bounds on the effective elastic moduli of polycrystals with orthorhombic symmetry, J. Appl. Phys. 50 (1979) 6290–6295, https://doi.org/10.1063/1.325768.
[41] J.P. Watt, L. Peselnick, Clarification of the Hashin-Shtrikman bounds on the effective elastic moduli of polycrystals with hexagonal, trigonal, and tetragonal symmetries, J. Appl. Phys. 51 (1980) 1525–1531, https://doi.org/10.1063/1.327804.
[42] R. Islam, F. Rahman, S. Bhattarai, H. Bencherif, M.K.A. Mohammed, R. Pandey, J. Madan, Photovoltaic Performance Investigation of Cs 3 Bi 2 I 9 - Based Perovskite 2 Solar Cells with Various Charge Transport Channels Using Density 3 Functional Theory and One-Dimensional Solar Cell Capacitance 4 Simulator Frameworks, 2023, https://doi.org/10.1021/acs.energyfuels.3c00540.
[43] J.V. Beitz, N.M. Edelstein, G.K. Liu, L.R. Morss, J. Solid State Chem.: Preface, Journal of Solid State Chemistry 178 (2005) 405, https://doi.org/10.1016/j.jssc.2004.10.001.
[44] F. Rahman, H. Rahman, R. Islam, M.K. Hossain, The optical and electronic properties of inorganic halide perovskite Sr3NCl3 under applied biaxial strain, J. Mater. Sci. (2012), https://doi.org/10.1007/s10853-023-08825-5.
[45] A.B. Shanto, F. Rahman, R. Islam, A. Ghosh, A. Azzouz-rached, H. Albalawi, Q. Mahmood, Investigating How the Electronic and Optical Properties of a Novel Cubic Inorganic Halide Perovskite , Sr 3 NI 3 Are Affected by Strain [Version 1 ; Peer Review : Awaiting Peer Review, 2023.
[46] A. Ghosh, M.F. Rahman, M.R. Islam, M.S. Islam, M. Amami, M.K. Hossain, A.B. Md Ismail, Inorganic novel cubic halide perovskite Sr3AsI3: strain-activated electronic and optical properties, Heliyon 9 (2023), e19271, https://doi.org/10.1016/j.heliyon.2023.e19271.
[47] M.F. Rahman, M.A. Rahman, M.R. Islam, A. Ghosh, M.A. Bashar Shanto, M. Chowdhury, M. Al Ijajul Islam, M.H. Rahman, M.K. Hossain, M.A. Islam, Unraveling the strain-induced and spin-orbit coupling effect of novel inorganic halide perovskites of Ca3AsI3 using DFT, AIP Adv. 13 (2023), https://doi.org/10.1063/5.0156961.
[48] F. Rahman, Investigation of a Novel Inorganic Cubic Perovskite Ca 3 PI 3 with Unique Strain-Driven Optical , Electronic , and Mechanical Properties, 2023, pp. 1–14, https://doi.org/10.1002/nano.202300066.
[49] A. Ghosh, F. Rahman, R. Islam, S. Islam, A. Ghosh, F. Rahman, R. Islam, Structural , Electronic and Optical Characteristics of Inorganic Novel Cubic Perovskite Sr 3 AsI, vol. 3, 2023.
[50] C. Hadenfeldt, H. Herdejürgen, Darstellung, kristallstruktur und thermisches verhalten der calciumphosphidchloride Ca2 - xP1 - xCl1+x ($0 \leq x \leq 0{,}18$) und Ca3PCl3, J. Less Common. Met. 124 (1986) 93–103, https://doi.org/10.1016/0022-5088(86)90480-7.
[51] H.J. Feng, Q. Zhang, Predicting efficiencies >25% A3MX3photovoltaic materials and Cu ion implantation modification, Appl. Phys. Lett. 118 (2021), https://doi.org/10.1063/5.0039936.
[52] M. Hasan, A.K.M. Akther Hossain, Structural, electronic and optical properties of strontium and nickel co-doped BaTiO3: a DFT based study, Computational Condensed Matter 28 (2021), e00578, https://doi.org/10.1016/j.cocom.2021.e00578.
[53] M. Hasan, A.K.M. Akther Hossain, First-principles calculations to investigate the structural, electronic, optical anisotropy, and bonding properties of a newly synthesized ThRhGe equiatomic ternary intermetallic superconductor, Results Phys. 42 (2022), 106004, https://doi.org/10.1016/J.RINP.2022.106004.

[54] M.K. Hossain, M.K.A. Mohammed, R. Pandey, A.A. Arnab, M.H.K. Rubel, K.M. Hossain, M.H. Ali, M.F. Rahman, H. Bencherif, J. Madan, M.R. Islam, D. P. Samajdar, S. Bhattarai, Numerical analysis in DFT and SCAPS-1D on the influence of different charge transport layers of CsPbBr3 perovskite solar cells, Energy Fuel. 37 (2023) 6078–6098, https://doi.org/10.1021/acs.energyfuels.3c00035.
[55] N. Titan, P. Hartono, H. Köbler, P. Graniero, M. Khenkin, R. Schlatmann, C. Ulbrich, A. Abate, Stability Follows Ef Fi Ciency Based on the Analysis of a Large Perovskite Solar Cells Ageing Dataset, 2023, https://doi.org/10.1038/s41467-023-40585-3.
[56] C.J. Rawn, M.W. Barsoum, T. El-raghy, A. Procipio, Structure of Ti 4 AlN 3 —a layered M 35, 2008, pp. 1785–1796.
[57] L. Kleinman, Deformation potentials in Silicon, Phys. Rev. 128 (1962) 2614.
[58] D.G. Pettifor, Theoretical predictions of structure and related properties of intermetallics, Mater. Sci. Technol. 8 (1992) 345–349, https://doi.org/10.1179/mst.1992.8.4.345.
[59] M. Jamal, S. Jalali Asadabadi, I. Ahmad, H.A. Rahnamaye Aliabad, Elastic constants of cubic crystals, Comput. Mater. Sci. 95 (2014) 592–599, https://doi.org/10.1016/j.commatsci.2014.08.027.
[60] M. Mattesini, R. Ahuja, B. Johansson, Cubic Hf3N4 and Zr3N4: a class of hard materials, Phys. Rev. B Condens. Matter 68 (2003) 2–6, https://doi.org/10.1103/PhysRevB.68.184108.
[61] A. Gueddouh, B. Bentria, I.K. Lefkaier, First-principle investigations of structure, elastic and bond hardness of FexB (x=1, 2, 3) under pressure, J. Magn. Magn Mater. 406 (2016) 192–199, https://doi.org/10.1016/j.jmmm.2016.01.013.
[62] P. Taylor, S.F. Pugh, XCII. Relations between the elastic moduli and the plastic properties of polycrystalline pure metals, Phys. Rev. 7 (1954) 823–843, 45.
[63] Z. Yang, D. Shi, B. Wen, R. Melnik, S. Yao, T. Li, First-principle studies of Ca-X (X=Si,Ge,Sn,Pb) intermetallic compounds, J. Solid State Chem. 183 (2010) 136–143, https://doi.org/10.1016/j.jssc.2009.11.007.
[64] V.V. Bannikov, I.R. Shein, A.L. Ivanovskii, Elastic properties of antiperovskite-type Ni-rich nitrides MNNi3 (M=Zn, Cd, Mg, Al, Ga, In, Sn, Sb, Pd, Cu, Ag and Pt) as predicted from first-principles calculations, Phys. B Condens. Matter 405 (2010) 4615–4619, https://doi.org/10.1016/j.physb.2010.08.046.
[65] Z. Sun, D. Music, R. Ahuja, J.M. Schneider, Theoretical investigation of the bonding and elastic properties of nanolayered ternary nitrides, Phys. Rev. B Condens. Matter 71 (2005) 3–5, https://doi.org/10.1103/PhysRevB.71.193402.
[66] S.I. Ranganathan, M. Ostoja-Starzewski, Universal elastic anisotropy index, Phys. Rev. Lett. 101 (2008) 3–6, https://doi.org/10.1103/PhysRevLett.101.055504.
[67] D.H. Chung, W.R. Buessem, The elastic anisotropy of crystals, J. Appl. Phys. 38 (1967) 2010–2012, https://doi.org/10.1063/1.1709819.
[68] F. Rahman, M. Islam, R. Islam, A. Ghosh, Q. Mahmood, Journal of Solid State Chemistry an investigation on strain-incited electronic and optical properties of novel inorganic cubic material Sr 3 AsCl 3, J. Solid State Chem. 328 (2023), 124341, https://doi.org/10.1016/j.jssc.2023.124341.
[69] M.C.P.M.D. Segall, R. Shah, C.J. Pickard, Population analysis of plane-wave electronic structure calculations of bulk materials, PHYSICAL REVIEW B 54 (1996) 317–320.
[70] R.S. Mulliken, Electronic population analysis on LCAO-MO molecular wave functions. I, J. Chem. Phys. 23 (1955) 1833–1840, https://doi.org/10.1063/1.1740588.
[71] M.I. Naher, M. Mahamudujjaman, A. Tasnim, R.S. Islam, S.H. Naqib, AbstAb-initio insights into the elastic, bonding, phonon, optoelectronic and thermophysical properties of SnTaS2, Solid State Sci. 131 (2022) 3–5, https://doi.org/10.1016/j.solidstatesciences.2022.106947.
[72] F.L. Hirshfeld, Bonded-atom fragments for describing molecular charge densities, Theor. Chim. Acta 44 (1977) 129–138, https://doi.org/10.1007/BF00549096.
[73] F. Rahman, R. Islam, A. Ghosh, Exploring the impact of strain on the electronic and optical properties of inorganic novel cubic perovskite Sr 3 PI 3, Phys. Scripta 98 (2023), 115105, https://doi.org/10.1088/1402-4896/acfce9.
[74] Y. Yun, D. Legut, P.M. Oppeneer, Phonon spectrum, thermal expansion and heat capacity of UO2 from first-principles, J. Nucl. Mater. 426 (2012) 109–114, https://doi.org/10.1016/j.jnucmat.2012.03.017.
[75] E.N. Koukaras, G. Kalosakas, C. Galiotis, K. Papagelis, Phonon properties of graphene derived from molecular dynamics simulations, Sci. Rep. 5 (2015), 12923, https://doi.org/10.1038/srep12923.